

# Pressure-field extraction from Lagrangian flow measurements: first experiences with 4D-PTV data

N. J. Neeteson<sup>1</sup> · S. Bhattacharya<sup>2</sup> · D. E. Rival<sup>1</sup> · D. Michaelis<sup>3</sup> · D. Schanz<sup>4</sup> · A. Schröder<sup>4</sup>

Received: 20 October 2015 / Revised: 11 April 2016 / Accepted: 19 April 2016 / Published online: 1 June 2016  
© Springer-Verlag Berlin Heidelberg 2016

**Abstract** As a follow-up to a previous proof-of-principle study, a novel Lagrangian pressure-extraction technique is analytically evaluated, and experimentally validated using dense 4D-PTV data. The technique is analytically evaluated using the semi-three-dimensional Taylor–Green vortex, and it is found that the Lagrangian technique out-performs the standard Eulerian technique when Dirichlet boundary conditions are enforced. However, the Lagrangian technique produces worse estimates of the pressure field when Neumann boundary conditions are enforced on boundaries with strong pressure gradients. The technique is experimentally validated using flow data obtained for the case of a free-falling, index-matched sphere at  $Re = 2100$ . The experimental data were collected using a four-camera particle tracking velocimetry measurement system, and processed using 4D-PTV. The pressure field is then extracted using both the Eulerian and Lagrangian techniques, and the resulting pressure fields are compared. Qualitatively, the pressure fields agree; however, quantitative differences are found with respect to the magnitude of the pressure minima on the side of the sphere. Finally, the pressure-drag coefficient is estimated using each technique, and the two techniques are found to be in very close agreement. A

comparison to a reference value from literature confirms that the drag coefficient estimates are reasonable, demonstrating the validity of the technique.

## 1 Introduction

This study is a follow-up to a previous work performed by Neeteson and Rival (2015), in which a novel technique was developed to extract time-resolved, three-dimensional pressure fields from Lagrangian flow data. The purpose of this follow-up study is to evaluate the performance of the existing technique, as well as to experimentally validate the results using representative high-density Lagrangian data. To this end, the technique is applied to two separate cases: first, an analytical case is utilized to evaluate the performance of the technique compared to that of a standard Eulerian pressure-extraction procedure. Second, the technique is validated by comparing the extracted pressure fields using the Lagrangian and Eulerian techniques for a sphere free-falling at a Reynolds number of 2100.

### 1.1 Background on Lagrangian flow measurement and pressure extraction

Lagrangian flow measurement techniques have become an increasingly active area of study in the literature. Several recent investigations into more sophisticated particle tracking velocimetry (PTV) algorithms have yielded very promising results. A few selected novel processing techniques which have been recently developed or proposed include: the ‘iterative particle reconstruction’ (IPR) technique developed by Wieneke (2013), the ‘Shake-The-Box’ (STB) technique developed by Schanz et al. (2013b, 2014), which is based on IPR, and a hybrid algorithm that combines

✉ N. J. Neeteson  
nathan.neeteson@queensu.ca

<sup>1</sup> Department of Mechanical and Materials Engineering,  
Queen’s University, Kingston, ON, Canada

<sup>2</sup> Department of Mechanical and Manufacturing Engineering,  
University of Calgary, Calgary, AB, Canada

<sup>3</sup> LaVision GmbH, Göttingen, Germany

<sup>4</sup> Department of Experimental Methods, German Aerospace  
Center (DLR), Institute of Aerodynamics and Flow  
Technology, Göttingen, Germany

tomographic reconstruction with particle tracking developed by Cornic et al. (2015). Historically, Lagrangian flow-measurement techniques have been limited compared to their Eulerian counterparts, with respect to the maximum optical particle density on the raw images. STB, or 4D-PTV, allows Lagrangian flow data to be collected using images with optical particle densities of up to 0.125 particles per pixel (ppp), which is more than a factor of two greater than the current maximum theoretical optical particle densities for PTV and IPR [up to  $10^{-2}$  ppp for PTV, as shown by Lüthi et al. (2005), up to  $5 \times 10^{-2}$  for IPR, as shown by Wieneke (2013)], and on par with the maximum theoretical optical particle density for tomographic PIV [up to 0.2, as shown by Lynch and Scarano (2015)]. As these flow measurement techniques become increasingly robust, it is imperative that novel techniques are developed to properly capitalize on the unique advantages inherent to Lagrangian flow data.

One area which warrants further investigation is pressure extraction using Lagrangian flow data. To date, there has been considerable investigation into the extraction of pressure fields from velocimetry data, and these investigations are documented in the literature review performed by van Oudheusden (2013). While many studies have used Lagrangian techniques in various stages of the pressure-extraction procedure, such as the studies performed by Violato et al. (2011), Novara and Scarano (2013) and Jeon et al. (2014), scattered Lagrangian flow data have universally been interpolated to a structured grid to perform spatial derivatives and the iterative integration necessary for pressure extraction. In the extraction of pressure fields from velocimetry data, the material derivative of velocity is of great importance. With Eulerian flow data, this quantity must be calculated using the following equation:

$$\frac{D\mathbf{u}}{Dt} = \frac{\partial \mathbf{u}}{\partial t} + (\mathbf{u} \cdot \nabla)\mathbf{u}, \quad (1)$$

where  $\mathbf{u}$  is the velocity,  $D\mathbf{u}/Dt$  is the material derivative, and  $\nabla$  is the vector differential operator. In the Lagrangian frame, the material derivative is equivalent to the acceleration of a particle and can be evaluated using the following equation:

$$\left(\frac{D\mathbf{u}}{Dt}\right)_i = \frac{d\mathbf{u}_i}{dt} = \frac{d^2\mathbf{x}_i}{dt^2}, \quad (2)$$

where the subscript  $i$  indicates that the velocity,  $\mathbf{u}_i$ , and position,  $\mathbf{x}_i$ , are Lagrangian and therefore refer to a specific particle rather than a static position in the field. It has been shown that evaluation of the material derivative using Lagrangian data produces more precise results than when using Eulerian data with the same time separation between frames (Violato et al. 2011; Novara and Scarano 2013; Jeon

et al. 2014). Since the advantages of using Lagrangian data for pressure extraction have been well established in the literature, the goal of the present study is to go a step further and determine whether it is advantageous to extract the pressure field in the Lagrangian frame, compared to simply interpolating the flow data and employing the standard Eulerian pressure-extraction techniques.

## 1.2 Lagrangian pressure extraction

Before proceeding with this section, it should be noted that this section, including Fig. 1, consists in large part of summarized material from the introduction to the previous investigation into this novel Lagrangian pressure-extraction technique (Neeteson and Rival 2015). This summarized material has been included in this work because it is critical to understanding the construction of the Lagrangian network, and the manner in which the pressure is extracted on this network.

In the proposed Lagrangian technique evaluated in this work, Poisson's equation for pressure is solved to extract the pressure field. The procedure of using Poisson's equation for pressure to extract the pressure field from experimental flow data was first employed over fifteen years ago by Gurka et al. (1999), using PIV data collected in a constricted pipe and an impinging air jet. In the first implementation of Poisson's equation for pressure on velocimetry data, finite-differences were used to evaluate the material derivative in an Eulerian frame, and a simple iterative solver was used to extract the pressure. Fujisawa et al. (2005) built on Gurka's technique by employing the successive over-relaxation (SOR) technique to solve Poisson's equation for pressure. In the interim, several subsequent studies have developed and employed more mathematically sophisticated methods of extracting the pressure field,

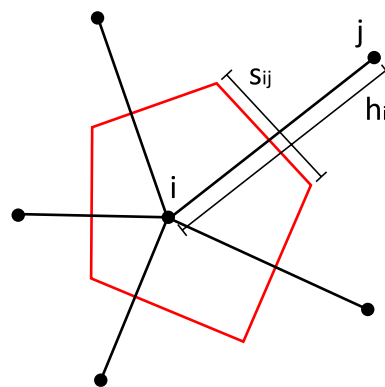


**Fig. 1** Example of a Voronoi tessellation in a two-dimensional space. The black dots represent data node locations. Black lines indicate connections between neighbours, red lines indicate Voronoi cell boundaries. Point  $i$  and neighbour  $j$  have a corresponding distance and Voronoi cell face size, labelled  $h_{ij}$  and  $s_{ij}$ , respectively

including studies which have: employed Taylor’s hypothesis and Reynold’s decomposition to separate the flow field and recast the governing equations (Laskari et al. 2014), allowed pressure fields to be extracted from single snapshots using the vorticity transport equations (Schneiders et al. 2014), and employed the Glowinski–Pironneau decomposition to separate the governing equations into a larger differential system in order to produce much more accurate estimates of the pressure field (Auteri et al. 2015). In the present study, however, the SOR method is used to iteratively solve Poisson’s equation for pressure, in a Lagrangian frame. This simpler method is chosen to first demonstrate the potential of the Lagrangian network, before moving on to investigations of more mathematically sophisticated pressure-extraction algorithms adapted to the Lagrangian network.

In a discrete Lagrangian frame, Poisson’s equation for pressure is a discrete boundary value problem described by the following equations:

$$\nabla^2 p_i = -\rho \left( \nabla \cdot \frac{D\mathbf{u}}{Dt} \right)_i, \text{ where } i \in \text{interior}, \tag{3}$$

$$\mathbf{n}_i \cdot \nabla p_i = \mathbf{n}_i \cdot \left( -\rho \left( \frac{D\mathbf{u}}{Dt} \right)_i + \mu (\nabla^2 \mathbf{u})_i \right), \tag{4}$$

where  $i \in \text{Neumann B.C.}$ ,

$$p_i = p_{D,i}, \text{ where } i \in \text{Dirichlet B.C.}, \tag{5}$$

where  $i$  is an index referring to a specific particle,  $p$  is the pressure,  $p_{D,i}$  is the prescribed pressure at a Dirichlet boundary,  $\mathbf{u}$  is the velocity,  $D\mathbf{u}/Dt$  is the material derivative (or acceleration of a particle),  $\mathbf{n}_i$  is the boundary normal vector at point  $i$  (if applicable),  $\rho$  is the density, and  $\mu$  is the dynamic viscosity. In order to solve this discrete boundary value problem without interpolation, several concepts are required.

In order to perform operations in the Lagrangian frame, a network must first be constructed on the field of particles, using the Delaunay triangulation and the Voronoi tessellation (Aurenhammer 1991). In short, these mathematical constructions allow a space to be filled with cells. Each cell corresponds to a particle, and particles that are linked in the network share a cell face. The distance between the neighbours,  $h$ , the area of the shared cell face,  $s$ , and the normal vector pointing from one particle to a neighbour,  $\hat{n}$ , are the network parameters that are used to perform vector calculus operations in the Lagrangian frame.

Next, it is necessary to be able to evaluate the divergence, gradient, and Laplacian operators on the network. The divergence and gradient are evaluated using the following expressions, which were originally derived by Neeteson and Rival (2015):

$$\nabla f_i = \frac{\sum_j [(f_i + f_j) s_{ij} \hat{n}_{ij}]}{\frac{1}{D} \sum_j (s_{ij} h_{ij})}, \tag{6}$$

$$\nabla \cdot \mathbf{F}_i = \frac{\sum_j [s_{ij} \hat{n}_{ij} \cdot (\mathbf{F}_i + \mathbf{F}_j)]}{\frac{1}{D} \sum_j (s_{ij} h_{ij})}, \tag{7}$$

where  $\nabla$  is the vector differential operator,  $f$  is a scalar field,  $\mathbf{F}$  is a vector field,  $D$  is the dimension of the space,  $\hat{n}_{ij}$  is the normalized vector pointing from  $i$  to  $j$ ,  $s_{ij}$  is the size of the cell face shared by  $i$  and  $j$ , and  $h_{ij}$  is the distance from  $i$  to  $j$ . For evaluation of the Laplacian operator, the following equation, derived by Sukumar and Bolander (2003), is used:

$$\nabla^2 f_i = \frac{\sum_j \left( \frac{s_{ij}}{h_{ij}} f_j \right) - f_i \sum_j \left( \frac{s_{ij}}{h_{ij}} \right)}{\frac{1}{2D} \sum_j (s_{ij} h_{ij})}. \tag{8}$$

Equation 6 combined with Eq. 4 allows for the Neumann boundary condition to be enforced. By rearranging Eq. 6, an expression can be obtained to obtain the pressure at a boundary point as a function of the pressure gradient, the network parameters, and the pressure at the point’s neighbours. Equation 7 is used to calculate the divergence of the material derivative, which is required in the calculation of the pressure source field. Finally, Eq. 8 can be rearranged to obtain an expression for calculating the pressure at a point as a function of the pressure source field, the network parameters, and the pressure at the point’s neighbours. This equation is used to iteratively update the value of the pressure field for interior points until convergence is achieved.

Finally, it is necessary to define a procedure for solving the discrete boundary value problem. In this technique, the SOR solver is used. Originally proposed by Young (1950), this technique includes a relaxation parameter that can be manipulated to either increase the convergence rate of a slowly converging integration, or to stabilize a divergent case. In this study, the relaxation parameter was left at unity. For additional background on the networking technique and integration procedure, the reader is referred to the study performed by Neeteson and Rival (2015), in which the technique was originally developed.

## 2 Analytical case: Eulerian versus Lagrangian pressure extraction

An analytical solution to the exact Navier–Stokes equations was used to evaluate the performance of the Lagrangian pressure-extraction technique. This evaluation was

performed by comparing the results of the Lagrangian pressure-extraction method to those of a typical Eulerian method. The purpose of this analysis was to evaluate the performance of the Lagrangian technique when beginning with Lagrangian flow data, compared to the standard pressure-extraction technique that has been observed in the literature. Therefore, the common starting point for each method was a scattered field of particles with known velocities and accelerations, equivalent in format to a post-processed PTV dataset. From this point, the pressure field was extracted from the flow data separately using the two methods.

In the Eulerian method, the pressure field was extracted using the following procedure: first, the flow data were interpolated from the scattered particles to a structured Eulerian grid using natural-neighbour interpolation (Sibson 1981). The source field and pressure-gradient field were then calculated using second-order finite-difference equations on interior nodes and first-order finite-difference equations on boundary nodes. Finally, a standard Poisson integration was performed to extract the pressure field. Choosing an appropriate pixel or voxel size for the structured grid is an important step when interpolating scattered data. In order to avoid both undersampling and oversampling, the voxel side length was chosen such that the overall number of voxels in the domain would be approximately equivalent to the number of particles in the original dataset. Therefore  $p$ , the side length of a voxel, was calculated using the following equation:

$$p = \left( \frac{V}{N_L} \right)^{1/3}, \quad (9)$$

where  $V$  is the volume of the domain, and  $N_L$  is the number of particles in the Lagrangian dataset. This voxel size estimate falls within guidelines published by Hengl (2006) when basing the pixel or voxel size on the density of the scattered data. Finally, since the volume was cubic, and since the number of voxels used must be an integer, the number of gridpoints in the Eulerian mesh was calculated by dividing the cube root of the total volume by the voxel side length, rounding it to the nearest integer, and cubing the result:

$$N_E = \left( \left\lfloor \frac{V^{1/3}}{p} \right\rfloor \right)^3, \quad (10)$$

where  $N_E$  is the number of gridpoints in the Eulerian frame, and  $\lfloor \cdot \rfloor$  is the nearest integer function. The Poisson integration was performed using the typical implementation found in the literature review performed by van Oudheusden (2013).

In the Lagrangian method, the pressure field was extracted using the following procedure: first, points were

added to the boundaries of the domain in order to explicitly enforce boundary conditions. Boundary points were added by sampling from the boundaries of the Eulerian structured grid, excluding the outer edges of each side of the cubic measurement volume. Therefore,  $((N_E)^{1/3} - 2)^2$  were added to each side of the domain to serve as boundary points. Next, the complete field of particles (data points and boundary points) was networked together using the Delaunay triangulation and Voronoi tessellation. Following this, the source field and pressure-gradient field were calculated on the Lagrangian network from the flow data. Finally, a Poisson integration was performed on the network to extract the pressure field. The optimal method for placing boundary points remains an area of active investigation. In the present work, points are placed on the boundary by sampling half of the points from the boundaries of the structured grid used in the Eulerian method.

## 2.1 The Taylor–Green vortex field

The analytical flow case used to compare the two methods was the semi-three-dimensional Taylor–Green vortex field. Derived by Taylor and Green (1937), the Taylor–Green vortex field is a closed-form, spatially periodic solution to the incompressible Navier–Stokes equations. This analytical flow case was chosen for testing for two reasons: first, and most importantly, the Taylor–Green vortex field has a known, analytical pressure field which varies in three dimensions. An exact reference pressure field allows extraction errors to be accurately estimated, and is critical in the evaluation of a pressure-extraction technique. The second reason the Taylor–Green vortex field was chosen for evaluation was the spatially periodic nature of the flow field. The topology of the flow allows a measurement domain containing multiple regions of high and low pressure, testing the technique’s ability to detect multiple structures in close proximity. Additionally, the topology of the flow field results in multiple flow structures intersecting the boundaries of the domain. A secondary purpose of this evaluation is to test the implementation of the Neumann boundary condition, and situations where strong pressure gradients are present on the boundary represent a worst-case scenario for this boundary condition.

The analytical form of the Taylor–Green vortex field is unstable, and it is typically used to simulate the generation of turbulence as the vortices in the field decay (Brachet et al. 1983; Brachet 1991; Shu et al. 2005). However, the velocity, material-derivative, and pressure fields can be described by closed-form expressions in the instant before the field begins to decay (denoted as  $t = 0$ ). Therefore, this case can be used to generate synthetic PTV data. Pressure extractions can be performed on this synthetic data, and the results can be compared to the exact analytical pressure

field. The velocity field at  $t = 0$  in the semi-three-dimensional Taylor–Green vortex field is given by:

$$u_x = V_0 \sin(x/L) \cos(y/L) \cos(z/L), \tag{11}$$

$$u_y = -V_0 \cos(x/L) \sin(y/L) \cos(z/L), \tag{12}$$

$$u_z = 0, \tag{13}$$

where  $V_0$  is the characteristic velocity of the flow, and  $L$  is the characteristic length scale of the flow. The corresponding instantaneous pressure field can be analytically derived using Poisson’s equation for pressure, and is given by:

$$p = \frac{\rho V_0^2}{16} \left[ \cos\left(\frac{2x}{L}\right) + \cos\left(\frac{2y}{L}\right) \right] \left[ \cos\left(\frac{2z}{L}\right) + 2 \right], \tag{14}$$

where  $\rho$  is the density of the fluid. Figure 2 shows a 2D slice of the pressure field at  $t = 0$  and  $z/L = 0$ , wherein the periodic nature of the flow field can clearly be observed. Finally, in order to assign acceleration values to particles in the synthetic datasets, the material-derivative field must be calculated. Typically, the material-derivative field would be calculated using the following vector equation:

$$\frac{D\mathbf{u}}{Dt} = \frac{\partial \mathbf{u}}{\partial t} + u_x \frac{\partial \mathbf{u}}{\partial x} + u_y \frac{\partial \mathbf{u}}{\partial y} + u_z \frac{\partial \mathbf{u}}{\partial z}. \tag{15}$$

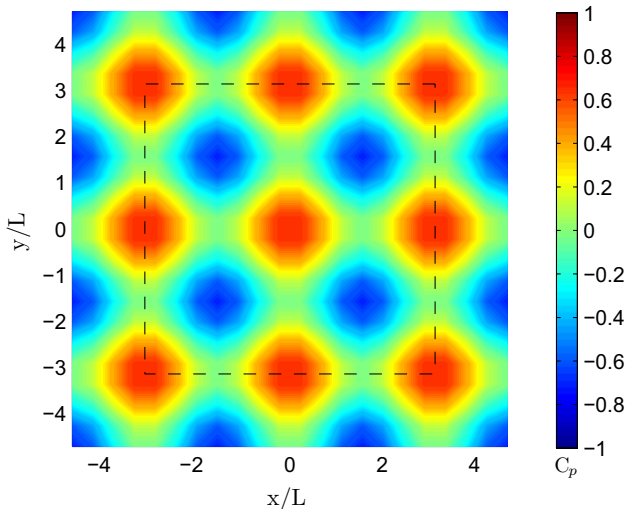


**Fig. 2** A 2-D slice (at  $z/L = 0$ ) of the analytical pressure field, in terms of the pressure coefficient, corresponding to the Taylor–Green vortex field at  $t = 0$ . This flow field is spatially periodic and extends infinitely in all directions. The *dotted line* indicates the intersection of the  $x - y$  plane with the smaller subset of the domain used to compare pressure-extraction accuracy between methods. This smaller domain was used in order to reduce the impact of erroneous results near boundaries, which can occur when Neumann boundary conditions are enforced.

However, since the Eulerian temporal derivatives of the velocity field ( $\partial \mathbf{u} / \partial t$ ) are nonzero and unknown, the above relations cannot be used. Instead, the closed-form expression for the instantaneous pressure field can be used to calculate the instantaneous material-derivative field by rearranging the incompressible, vector Navier–Stokes equation:

$$\frac{D\mathbf{u}}{Dt} = -\frac{1}{\rho} \nabla p + \frac{\mu}{\rho} \nabla^2 \mathbf{u}, \tag{16}$$

where  $\mu$  is the dynamic viscosity of the fluid. For all of the tests conducted in this work, the Reynolds number was fixed at  $Re = 10^4$  by choosing  $L = 1$  m,  $V_0 = 10$  m/s,  $\rho = 1$  kg/m<sup>3</sup>, and  $\mu = 10^{-3}$  kg/(m s).

Synthetic tests were conducted in a cubic region of side length  $3\pi$  centred at the origin of the coordinate system. This domain was selected to ensure that a sufficient number of vortex structures were contained within the volume to adequately test each pressure extraction method. Moreover, the selected domain size allowed a smaller sub-domain to be defined that itself contained several vortex structures. This sub-domain, a smaller, cubic region with side length  $2\pi$ , centred at the origin, was used to quantify the pressure-extraction error in each case. Excluding points near the boundaries of the domain is done to mitigate the influence of erroneous aberrations in the extracted pressure field, which are more likely to occur near domain boundaries in both the Eulerian and Lagrangian methods.

In order to generalize the results of the analysis, it is most useful to discuss pressure fields in terms of the dimensionless pressure coefficient. The pressure coefficient is defined as:

$$C_p = \frac{p - p_0}{\frac{1}{2} \rho V_0^2}, \tag{17}$$

where  $p_0$  is some reference pressure and was defined as  $p_0 = 0$  for the purposes of this analysis. For the remainder of the discussion of the analytical test case, all pressure fields will be shown in terms of the pressure coefficient. Spatial particle densities in the analytical case will be shown in terms of the normalized spatial particle density, defined as:

$$N^* = \frac{NL^3}{V}. \tag{18}$$

Using the STB tracking algorithm with a four megapixel camera would allow for up to approximately  $4 \times 10^5$  particles to be tracked. Assuming the measurement volume is approximately ten times the volume of the characteristic volume of the flow structures of interest, this results in a normalized spatial particle density of approximately  $N^* \approx 4 \times 10^4$ .

### 2.2 Results of Eulerian versus Lagrangian comparison

First, synthetic Lagrangian datasets were created across a range of normalized spatial particle densities. The pressure field was then extracted from these datasets using both the Eulerian and Lagrangian methods, using both Dirichlet and Neumann boundary conditions. Since Eulerian and Lagrangian methods produce different distributions of errors, the most robust criterion for comparison between the cases is the 95th percentile of error in each pressure field. The error in the extracted pressure field was calculated at each particle or grid point using the following equation:

$$\Delta C_p = |C_{p,estimated} - C_{p,analytical}|, \tag{19}$$

where  $\Delta C_p$  is the normalized pressure-extraction error field,  $C_{p,estimated}$  is the estimated or extracted pressure field,  $C_{p,analytical}$  is the analytical pressure field, and  $|\cdot|$  is the absolute value function. Then, the 95th percentile was calculated using the nearest rank method, using the following equations:

$$n = \lceil .95 \times N \rceil, \tag{20}$$

$$\Delta C_{p,95\%} = \Delta C_{p,ordered}(n), \tag{21}$$

where  $n$  is the ordinal rank corresponding to the 95th percentile,  $\lceil \cdot \rceil$  is the ceiling function,  $N$  is the total number of data points,  $\Delta C_{p,ordered}$  is an ordered list of the error in terms of pressure coefficient at all points within the sub-domain, and  $\Delta C_{p,95\%}$  is the 95th percentile of pressure-extraction error in the field.

For each case, at each normalized spatial particle density, the pressure field was extracted from five different randomly seeded particle fields, and the resulting error estimates were averaged together. Figure 3 shows the results

of this analysis. Initially, for all four cases the relationship between the pressure-extraction error and the normalized spatial particle density follows the same power-law relationship observed in the previous investigation into this technique (Neeteson and Rival 2015). However, the error in the pressure fields extracted using the Lagrangian method with Neumann boundary conditions plateaus at  $\delta C_{p,95\%} \approx 0.12$ , diverging from the expected power-law relationship at  $N^* \approx 75$ , which is several orders of magnitude lower than what is presently achievable using 4D-PTV. A linear regression analysis performed on the Dirichlet boundary condition case yielded the following power-law relations for the Lagrangian and Eulerian methods:

$$\Delta C_{p,95\%} \approx \begin{cases} 3.1(N^*)^{-0.63} & : \text{Eulerian, Dirichlet BC} \\ 1.5(N^*)^{-0.61} & : \text{Lagrangian, Dirichlet BC} \end{cases} \tag{22}$$

For both methods, the relationship between the pressure-extraction error and normalized spatial particle density agrees with the results obtained in the previous investigation of this technique (Neeteson and Rival 2015), finding a power-law relationship between the pressure-extraction error and the normalized spatial particle density. Furthermore, when the Dirichlet boundary condition is applied, the 95th percentile of error in the Lagrangian extracted pressure fields is approximately half of that in the Eulerian fields for a given spatial particle density. Therefore, based on this analysis, it can be stated that the Lagrangian method produces more accurate pressure fields than the basic Eulerian method when Dirichlet boundary conditions are enforced on the boundaries. While the Lagrangian method with Neumann boundary conditions case initially follows the expected power-law relationship with normalized spatial particle density, the error plateaus at  $C_{p,95\%} \approx 0.12$

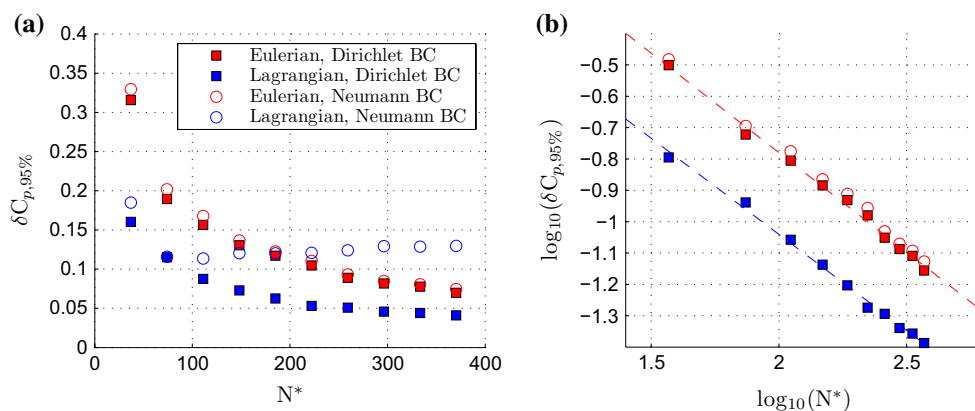


**Fig. 3** **a** Plot of the 95th percentile of pressure-extraction error (within the previously defined sub-domain) in terms of the pressure coefficient versus the normalized spatial particle density for four test cases. **b** Log–log plot of the 95th percentile of pressure-extraction error versus the normalized spatial particle density. The Lagrangian

method, Neumann boundary condition case has been excluded from the log–log plot due to its non-conformity to the expected power-law relationship. The *dashed lines* show the results of the linear regression analysis on the Dirichlet boundary condition cases (*red* for Eulerian, *blue* for Lagrangian)

where  $N^* \approx 75$ . Beyond this point, there appears to be no gain in pressure-field accuracy as the density of the data is increased. Therefore, when Neumann boundary conditions are enforced on the boundaries, the Eulerian method appears to out-perform the Lagrangian method at higher normalized spatial particle densities.

A plateau of pressure-extraction accuracy as the number of particles is increased is highly irregular. To comment on the possible origin of errors in the extracted pressure fields in each case, sample pressure fields, and corresponding error fields, are presented in Figs. 4 and 5. Figure 4 shows sample pressure fields, and their corresponding error fields, extracted using the Eulerian and Lagrangian methods with Dirichlet boundary conditions for  $N^* \approx 370$ . In this figure, it can be observed that within the interior sub-domain, the Lagrangian pressure field displays overall less pressure-extraction error than the Eulerian pressure field. Moreover, the Lagrangian pressure field is more consistent in its accuracy when compared to the Eulerian pressure field. In both cases, the error in the extracted pressure field is largest in regions of high or low pressure, as expected.

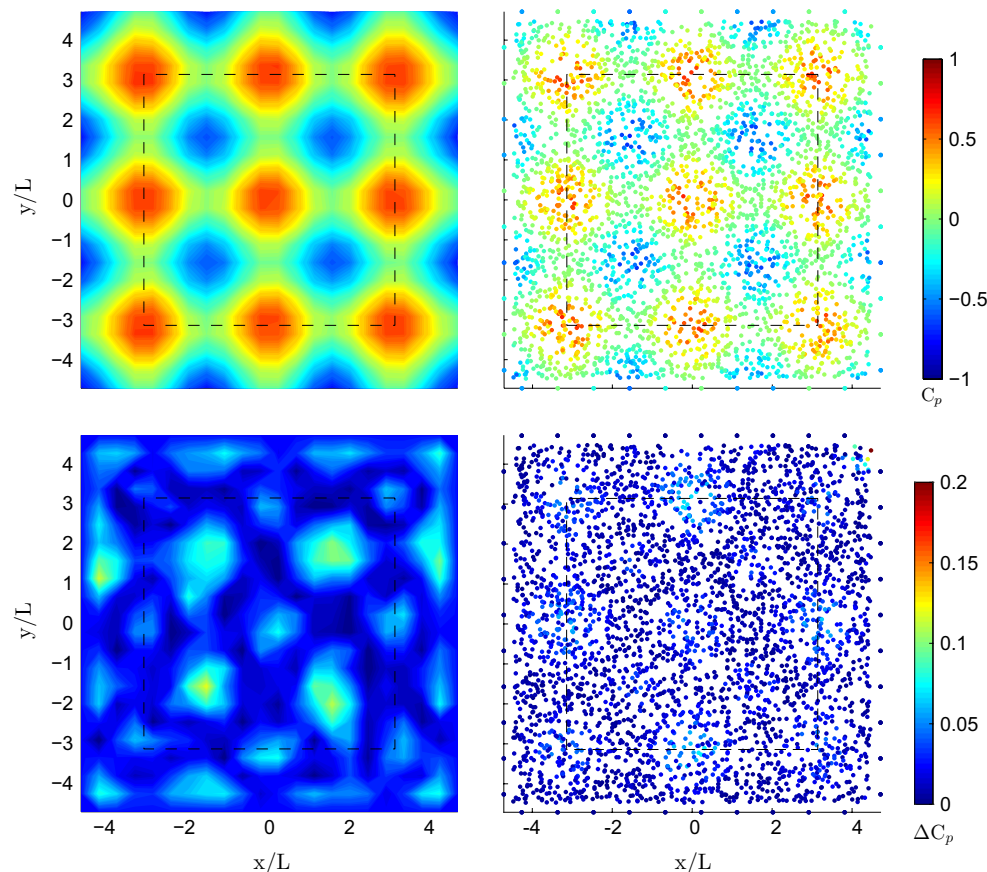


**Fig. 4** Sample extracted pressure fields, and corresponding error fields, for  $N^* \approx 370$  with Dirichlet boundary conditions. The *top row* shows the extracted pressure field, while the *bottom row* shows the corresponding error field. The *left column* displays results from

Figure 5 shows sample pressure fields, and their corresponding error fields, extracted using the Eulerian and Lagrangian methods with Neumann boundary conditions for  $N^* \approx 370$ . The cause of the increased error in the Lagrangian domain is immediately apparent when Figs. 4 and 5 are compared. In each figure, the error in the pressure field extracted using the Eulerian method is roughly equivalent in both form and magnitude. This result suggests that in the basic Eulerian method, the type of boundary conditions implemented have little influence on the overall accuracy of the extracted pressure field away from the boundaries. However, the error in the pressure fields extracted using the Lagrangian method differs greatly, depending on which boundary conditions are employed. It can be observed in Fig. 5 that there is a relatively high amount of pressure-extraction error on the boundaries of the domain when a Neumann boundary condition is employed. The error in the extracted pressure field is highest in locations where a significant flow structure is cut off by the boundary, and is relatively low in locations where no such structure is present on the boundary.

the Eulerian frame, and the *right column* displays results from the Lagrangian frame. All pressure fields shown are a 2D slice at  $z/L = 0$ , in the Lagrangian frame the slice is constructed by compressing points within the range  $-0.5 < z/L < 0.5$  to a plane

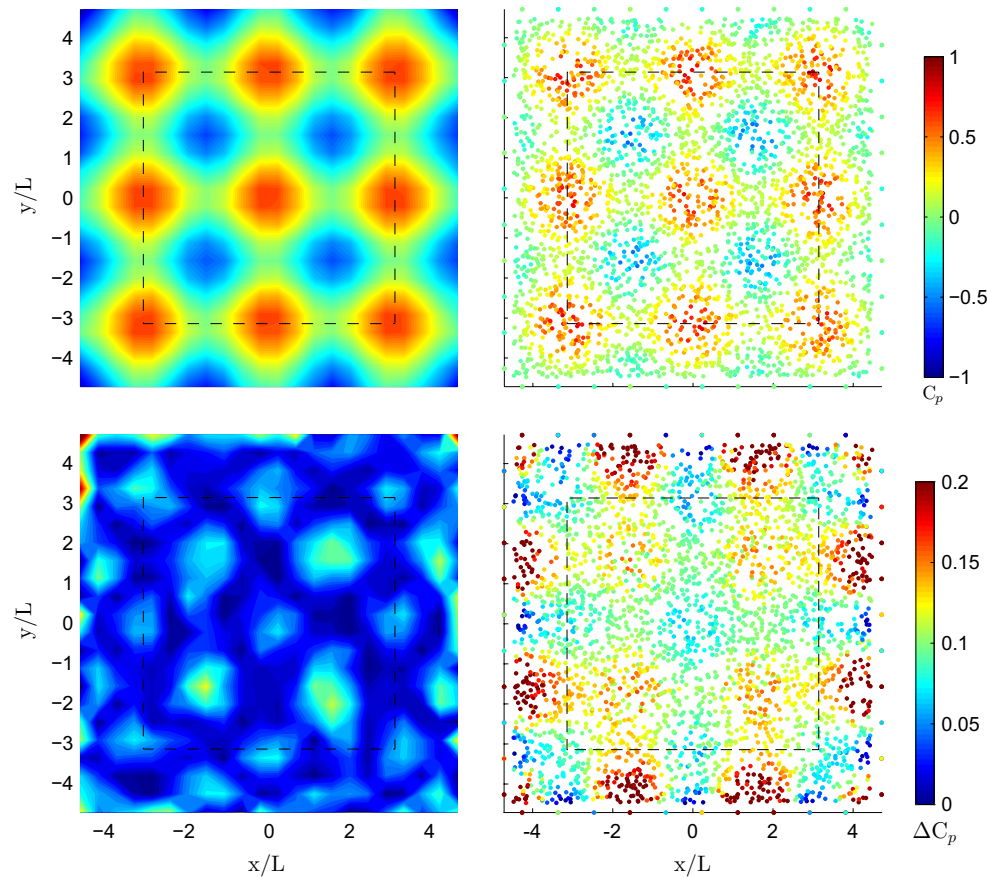


**Fig. 5** Sample extracted pressure fields, and corresponding error fields, for  $N^* \approx 370$  with Neumann boundary conditions. The *top row* shows the extracted pressure field, while the *bottom row* shows the corresponding error field. The *left column* displays results from the

Eulerian frame, and the *right column* displays results from the Lagrangian frame. All pressure fields shown are a 2D slice at  $z/L = 0$ , and in the Lagrangian frame the slice is constructed by compressing points within the range  $-0.5 < z/L < 0.5$  to a plane

Due to the nature of an iterative Poisson solver, relatively high errors in one location of the field will diffuse through the network and adversely impact the accuracy of the solution in neighbouring regions. This effect can be clearly observed in Fig. 5: in regions of low pressure on the boundary of the domain, there are relatively high errors in the extracted pressure field. The errors on the boundary of the domain adversely influence the accuracy of the solution at their neighbours, and this effect diffuses throughout the domain of integration. The error field observed in the Lagrangian domain in Fig. 5 can be seen to be a combination of this diffusion of solution error and the analogous error field in Fig. 4. Therefore, it can be argued that observed inaccuracy of the extracted pressure field using the Lagrangian method with Neumann boundary conditions is due to a combination of the following factors: first, relatively high errors occur in the extracted pressure field where strong flow structures intersect the domain boundary. Then, these errors are diffused throughout the domain, due to the nature of the iterative Poisson solver.

It is important to note at this point that the chosen analytical test case represents a near-worst-case scenario in terms of the implementation of Neumann boundary conditions. The periodic nature of the flow field guarantees that flow structures will be present on the boundaries of the domain, regardless of the selected synthetic measurement domain. Additionally, the flow structures cut off by the boundaries are identical in size and strength to the structures contained within the synthetic measurement domain. In practice, when acquiring flow data for the purposes of pressure extraction, it would be desirable to choose a measurement volume such that the boundaries of the domain do not cut off significant structures in the flow, if possible. In such cases, either a Dirichlet boundary condition could be employed, assuming the flow on the boundaries is in free-stream, or the pressure gradient used in the Neumann boundary condition would be minimal. However, it will often not be possible to choose such an optimal measurement domain with favourable boundary conditions. If significant flow structures are found to exist on a Neumann



boundary, and the Lagrangian method is used in its current implementation, it is highly probable that the accuracy of the solution on the domain would be adversely affected.

The following general conclusions can be drawn based on the tests performed using the analytical test case:

First, as expected, Dirichlet boundary conditions have been observed to produce better estimates of the overall pressure field than Neumann boundary conditions in both cases. When Dirichlet boundary conditions are implemented properly, the pressure that is set on the boundaries is correct. This results in zero pressure-extraction error on the Dirichlet boundary. However, even when the Neumann boundary conditions are implemented optimally, the pressure-extraction error on the boundary will be nonzero. The pressure gradient on the boundary is calculated from the data using discretized expressions, so in addition to whatever underlying uncertainty there is in the data, there is an added layer of discretization error in the estimate of the pressure gradient. This error in the pressure gradient then propagates to the estimate of the pressure on the boundary. Finally, the errors diffuse throughout the domain in the integration process. Therefore, so long as the pressure gradient is calculated from the data itself, rather than being set using some sort of external knowledge about the flow field, Dirichlet boundary conditions will result in lower pressure-extraction error than Neumann boundary conditions.

Second, in situations where the Dirichlet boundary condition can be employed on the boundaries of the measurement volume, the Lagrangian pressure-extraction method will produce more accurate estimates of the pressure field than the Eulerian pressure-extraction method. This is observed in Fig. 3, where the Lagrangian method consistently out-performs the Eulerian method when using Dirichlet boundary conditions. Third, in situations where significant flow structures are present at the boundary of the measurement volume, the accuracy of the pressure field extracted using the Lagrangian method will suffer due to a combination of high errors at the intersection of the flow structure and the boundary, and the diffusion of these errors through the domain. Figure 5 clearly shows that the diffused error from the flow structures at the boundaries is the dominant source of error in the pressure field. In the current implementation of the technique, this error source will dominate whenever there are strong pressure gradients on the domain boundary.

Finally, in situations where the Neumann boundary condition must be employed on the boundaries of the measurement volume, but the pressure gradient at the boundary is minimal and no significant flow structures exist near or on the boundaries, the Lagrangian pressure-extraction method will most likely function in a similar manner as it would with Dirichlet boundary conditions. The magnitude of the diffused error from the boundary is proportional to the

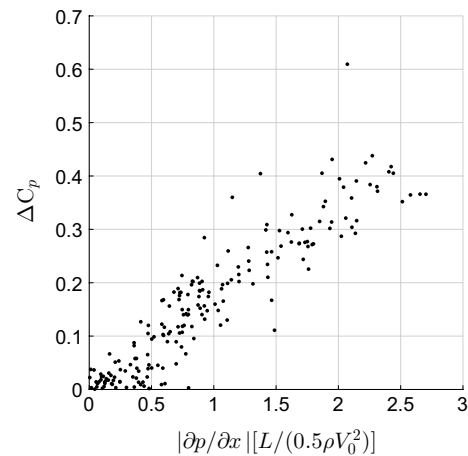


**Fig. 6** The normalized pressure-extraction error is plotted against the normalized absolute pressure gradient in the  $x$ -direction for all of the points along the east boundary ( $x^+$ ) of the domain for the pressure field extracted in the Lagrangian domain, with Neumann boundary conditions, and  $N^* \approx 370$ . The pressure gradient is normalized in a similar manner as the pressure coefficient, albeit multiplied by the characteristic length scale to fully non-dimensionalize

strength of the pressure gradient at the boundary, see Fig. 6. Therefore, if the pressure gradient is minimal at the boundary, then the truncation error, which is dependent on the particle density, will once again dominate. However, it is clear that in situations where strong pressure gradients can be expected to coincide with boundaries of the measurement domain, the current proposed Lagrangian technique will produce an estimate of the pressure field which is less accurate than that of an Eulerian technique. This limitation makes it clear that the proposed technique requires further investigation, in order to determine the root cause and assess whether modifications can be made to the boundary condition implementation strategy in order to remedy this weakness.

### 3 Experimental case

In addition to evaluating the technique relative to a typical Eulerian procedure with analytical data, experimental data were used to qualitatively and quantitatively validate the results of the technique in practice. In order to collect the type of high-quality, high-density Lagrangian flow data required for Lagrangian pressure extraction, without performing phase-averaging, it was necessary to employ a more advanced tracking algorithm than standard PTV. Experimental data were processed using Shake-The-Box, a novel volumetric particle tracking algorithm developed by Schanz et al. (2013b), more formally known as 4D-PTV. In

this section, the experimental methods are described, and the resulting experimental data are analysed.

### 3.1 Experimental methods

The experiment was performed at Queen's University in a free-surface octagonal water tank, with a width of 60 cm and filled with water to a height of 52 cm. A hydrogel sphere, with a diameter of  $4.318 \pm 0.001$  cm, was manually released from rest at a submerged location above the measurement volume. The sphere was observed to be travelling at an approximately constant velocity ( $V_s$ ) of 0.049 m/s as it travelled through the optical measurement volume. The hydrogel sphere, produced by M2 Polymer Technologies, was composed of an acrylic-acrylamide co-polymer and is referred to as a 'super-absorbent polymer' (SAP) sphere. SAP spheres are soaked in water for 24–48 h prior to testing, in order to saturate the structure with water. After soaking, the sphere is predominantly composed of water, and therefore the refractive index and density of the sphere are very closely matched to that of water. Figure 7 shows a picture and diagram of the experimental set-up, and Table 1 shows a list of the relevant experimental parameters.

Using a SAP sphere as the model provides two benefits critical to this experiment: first, with the hydrogel sphere's index of refraction closely matched to that of water, light reflected from particles is not occluded or significantly refracted by the spherical model. This allows imaging of the entire flow field around the sphere. Second, the closer the densities of the sphere and water are, the slower the free-fall descent of the sphere will be. A low descent velocity is important in the current experimental set-up, as the temporal frequency of data collection is constrained by the amount of light in the measurement volume, and this in turn limits the maximum trackable particle velocity.

The octagonal tank was seeded with 100- $\mu\text{m}$ , silver-coated, hollow glass spheres with a density of approximately  $1000 \text{ kg/m}^3$ . Tracking errors were estimated to be less than 1 % of the characteristic velocity, based on the Stokes number of the seeding particles satisfying  $\text{Stk} \ll 10^{-3}$  (Raffel et al. 2007). The temperature of the water in the octagonal tank was reduced to  $15.2 \text{ }^\circ\text{C}$  in order to further slow the descent of the sphere. At this temperature, with a characteristic length of 4.32 cm and a characteristic velocity of 4.9 cm/s, the Reynolds number of the experimental case was approximately  $Re \approx 2100$ . The measurement domain was limited to a circular cylinder, oriented in the direction of travel of the spherical model, with a diameter of  $d \approx 8.0$  cm and a height of  $h \approx 6.8$  cm. The measurement domain was illuminated using an HID light source which was mounted underneath the table, with a hole cut in the table wide enough to allow the beam of light to pass up

**Table 1** Parameters of the experimental case used for pressure extraction

model		SAP sphere
medium		Water
Model diameter (m)	$D_s$	0.0432
Model radius (m)	$R_s$	0.0216
Measured descent velocity (m/s)	$V_s$	0.049
Temperature ( $^\circ\text{C}$ )	$T$	15.2
Reynolds number	$Re$	$\approx 2100$

through the measurement volume. A Cartesian coordinate system was used, with the  $z$ -axis aligned with the direction of travel of the sphere. The  $x$ - and  $y$ -axes were defined by the orientation of the calibration target.

Figure 7a shows the experimental set-up. Four pco. edge sCMOS high-speed cameras were used, each recording a field of view of  $8.0 \times 6.8 \text{ cm}^2$  with a resolution of  $2560 \times 2160$  pixels, at a framerate of 100 Hz. First, the camera array was calibrated using a standard pinhole calibration. Next, the volume self-calibration technique developed by Wieneke (2008) was used to refine the calibration. This technique has been shown to produce much more accurate camera system calibrations when combined with the standard pinhole calibration technique utilized in more basic particle tracking packages (Wieneke 2008). Finally, an optical transfer function (OTF) is calibrated (Schanz et al. 2013a). The OTF is particularly important in STB, since it attempts to account for distortions of particle shapes on the camera images and allows for more accurate particle triangulations. Images recorded by the camera array were then processed using the Shake-The-Box (STB) processing technique developed by Schanz et al. (2013b). A general description of the STB-processing work-flow is given below, for more details refer to the studies performed by Schanz et al. (2013b, 2014).

Under the assumption that the trajectories of (nearly) all particles within the system are known for a certain number of time-steps  $t_m$  to  $t_n$ , the STB-method scheme for the single time-step  $t_{(n+1)}$  is as follows:

1. Fit a function (polynomial) to the last  $n$  positions of every tracked particle;
2. Predict the position of the particle in  $t_{(n+1)}$  by evaluating the fitted polynomial;
3. Shake the particles to their correct position and intensity, eliminating the error introduced by the prediction—this step is realized using an image matching technique;
4. Find new particles, entering the measurement domain, on the residual images;
5. Shake all particles again to correct for residual errors;

6. Remove particles either if leaving the volume or if intensity falls below the threshold;
7. Iterate steps 4, 5 and 6, if necessary;
8. Add new tracks for all new particles that are identified within four consecutive time-steps.

Following this scheme, the algorithm can work its way through an entire time-series, consisting of possibly thousands of images. The effort needed for every single time-step is low, as the system is largely pre-solved after the prediction-step, and only minor deviations have to be corrected. However, the knowledge of a vast majority of particle tracks is not a given, since at the beginning the method has to start from scratch. Therefore, the first few time-steps receive an enhanced treatment in order to quickly identify as many particle tracks as possible.

In the present experimental case, this initialization phase lasted for the first four time-steps. In each of these time-steps, the following procedure was carried out: first, four standard triangulation operations were performed, followed by five shake iterations. Next, two times four triangulations were executed using a reduced camera system (iteratively leaving one camera out in order to reduce effects of particle overlap and/or decalibrations), again each followed by five shake iterations. During normal operations, the procedure consisted of two normal triangulations and one reduced-camera-system triangulation, each followed by five shake iterations. Particles are deleted from the tracking system if the intensity falls below 0.12 times the average particle intensity. In this case, it is assumed that the particle track

was lost. Due to the relatively low seeding density (approximately 0.005 ppp on average) and lack of particle motion in the initialization stage, no particle trajectory predictor was necessary in the initialization stage. Table 2 displays the relevant parameters used for the STB algorithm during normal operation in the present experimental case.

Four passes of the STB procedure were employed on the collected images: as soon as the algorithm has processed the whole sequence of 500 images, time can be reversed and the algorithm walks backwards—elongating existing tracks backwards in time and possibly connecting existing track fragments. Figure 8 shows the number of tracked particles in each time-step for the different passes, as well as track length statistics for the present experimental case. In the final dataset, 696 particles are tracked over the whole 500 time-steps, and the average track length is 49.4 time-steps. The presence of the sphere (and therefore a region void of particles within the measurement area) is documented by the decrease in tracked particles for images 60–280.

As this technique has only recently been developed, robust methods of estimating the uncertainty in the flow data are not yet available. Currently, the best method for estimating the uncertainty in the particle positions, velocities, and accelerations is to use the average deviation of particle positions from the temporal fit applied to the tracks during the STB processing. Using third-order polynomials fit to nineteen time-steps, the standard deviation in the polynomial fit was 0.3 pixels in the current case. This uncertainty is relatively large compared to ideal

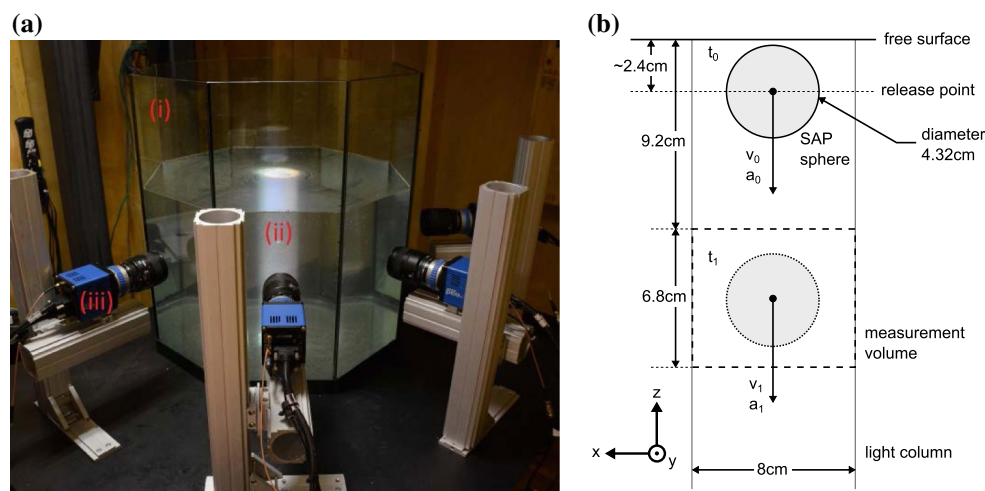


**Fig. 7** **a** A photograph of the experimental apparatus. Labelled are (i) the octagonal tank, (ii) the cylindrical light column produced by the HID light source attached underneath the table, and (iii) one of the four pco.edge sCMOS cameras used to capture images for PTV. All four cameras are aimed perpendicular to the walls of the octagonal tank in order to minimize refractions and reflections on the cam-

era images. **b** A diagram of the experimental set-up. The sphere is released from rest from a submerged position above the measurement domain. Once it has entered the measurement domain, the sphere has ceased accelerating, or the acceleration is negligible, and falls through the domain at an approximately constant velocity

volume-self-calibrated STB output [0.07 pixels for a signal-to-noise ratio of 10, and 0.13 pixels for a signal-to-noise ratio of 5 (Schanz et al. 2013b)]. There are several reasons for this: first, the quality of the calibration in the current experimental set-up was adversely affected by the insufficient light intensity provided by the HID light source. In order to allow enough light to hit the sensor to provide an acceptable signal-to-noise ratio (SNR), the aperture could not be closed enough to contain the entire measurement domain within the depth of field. This resulted in poor calibration in the near- and far-field for each camera, adversely affecting the calibration on all boundaries of the measurement domain. Second, many particles adhered to the surface of the sphere. These particles appeared ‘patchy’ on the raw images and potentially detrimentally impacted the tracking of any nearby particles, by occluding them on the camera sensors. Finally, particles travelling near the velocity limit of the PTV system ( $V_{\max} \approx 6.25$  cm/s) tended to become elongated on the camera images due to streaking. This elongation increased the difficulty in triangulation of the particles’ positions, contributing to the overall particle location uncertainty.

Starting from a pixel uncertainty of  $\pm 0.3$  pixels in the system, the overall uncertainty in the particle positions can be calculated by translating the pixel uncertainty into spatial uncertainty using the resolution and field of view of the cameras:

$$\text{Spatial uncertainty} = \left( \frac{\text{Spatial camera width}}{\text{Pixel camera width}} \right) \times (\text{Pixel uncertainty}) \quad (23)$$

The uncertainty in the velocity and acceleration data can then be calculated by applying error propagation to the particle uncertainty: assuming that the spatial uncertainty dominates the temporal uncertainty ( $\delta x / \Delta x \gg \delta t / \Delta t$ ),

**Table 2** Parameters of the STB-processing algorithm

Allowed triangulation error	1.7 pixel
Triangulation threshold	250 counts
Search radius for finding new tracks around particles which have a predictor	6 pixel
Search radius for finding new tracks around particles which have NO predictor	21 pixel

the uncertainty in a temporal derivative will be equal to the framerate multiplied by the uncertainty of the derived quantity:

$$\delta u = \left( \frac{1}{\Delta t} \right) \delta x, \quad (24)$$

$$\delta Du/Dt = \left( \frac{1}{\Delta t} \right)^2 \delta x, \quad (25)$$

where  $\Delta t$  is the period of a single frame, or  $\Delta t^{-1}$  is the framerate. The uncertainty in particle positions ( $\delta x$ ), velocities ( $\delta u$ ), and accelerations ( $\delta Du/Dt$ ) are then:

$$\delta x = \left( \frac{8(10^{-2}) \text{ m}}{2560 \text{ px}} \right) (\pm 0.3 \text{ px}) \approx \pm 1(10^{-5}) \text{ m}, \quad (26)$$

$$\delta u = \left( \frac{1}{0.01 \text{ s}} \right) \left( \frac{8(10^{-2}) \text{ m}}{2560 \text{ px}} \right) (\pm 0.3 \text{ px}) \approx \pm 1(10^{-3}) \text{ m/s}, \quad (27)$$

$$\delta Du/Dt = \left( \frac{1}{0.01 \text{ s}} \right)^2 \left( \frac{8(10^{-2}) \text{ m}}{2560 \text{ px}} \right) (\pm 0.3 \text{ px}) \approx \pm 1(10^{-1}) \text{ m/s}^2. \quad (28)$$

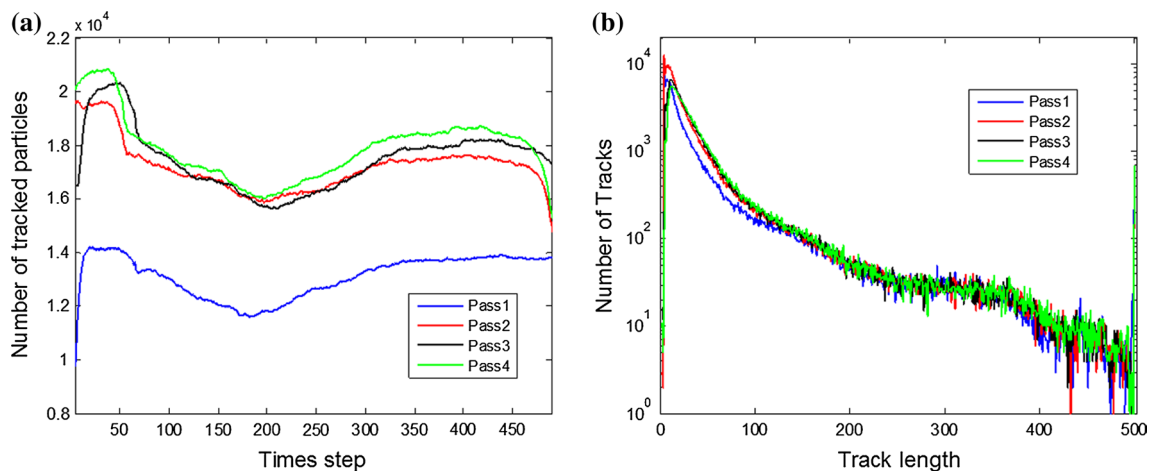


**Fig. 8** **a** Number of tracked particles over time for each pass through the dataset. **b** Track length statistics for each pass through the dataset

Finally, the characteristic error in the particle positions and velocities can be determined by calculating the ratio of the uncertainty to the characteristic length or velocity. The characteristic uncertainty in the position field is  $\delta x/R_s \approx \pm 0.05\%$ , and the characteristic uncertainty in the velocity field is  $\delta u/V_s \approx \pm 2\%$ .

### 3.2 Experimental results: sphere position, lagrangian tracks

The first step in the data analysis was to determine the spatial position of the hydrogel sphere at each time-step. Since the hydrogel sphere was index-matched to the water, its location could not be accurately determined from the raw images. Instead, the sphere was located using the Lagrangian particle field. Seeding particles were distributed evenly throughout the measurement volume. Since the surface of the hydrogel sphere was impermeable, it created a spherical region devoid of seeding particles as it travelled through the measurement domain. Using a MATLAB script to calculate the number of particles contained within a moving spherical volume, the position of the hydrogel sphere could be estimated for each time-step. Since tracked particles are not always present right up to the boundaries of the sphere, the tracking technique was only able to estimate the position of the sphere to within  $\pm 1$  mm. Figure 9a displays the tracked location of the sphere for  $1.2 < t [\text{s}] < 1.7$ , as well as a line of best fit produced by a linear regression on the tracking data. Due to the technique used to track the sphere, it could only be tracked within a space of approximately

25 mm (when it was fully enclosed within the measurement domain). The sphere was observed to be falling at a constant velocity. A linear regression estimated the descent velocity of the sphere to be  $V_s = 0.049$  m/s, and the linear fit matches the observed data quite closely.

Figure 9b shows Lagrangian particle tracks in the reference frame of the sphere, translated from the original three-dimensional Cartesian coordinate system to a cylindrical axisymmetric coordinate system for easier visualization. A stagnation point is observed at the leading point. Relative to the sphere, the flow is accelerated to approximately 1.4 times the descent velocity as it passes by the side of the sphere. It can be seen that the boundary layer separates from the body at approximately  $125^\circ$  from the front leading stagnation point, forming a circulating wake region on the trailing end of the sphere. The separated boundary layers appear to be in the process of reattaching approximately  $1.5R_s$  downstream from the trailing point on the sphere. Particle tracks in the dataset lasted for approximately 45 time-steps on average. In each time-step, approximately 15,000 individual particles were tracked. Based on the volume of the measurement domain and the characteristic length of the flow case, the corresponding normalized spatial particle density in a given time-step is  $N^* \approx 4000$ .

### 3.3 Experimental results: pressure-field analysis

The next step in the data analysis was to extract the pressure field around the sphere for every time-step where the sphere was surrounded by tracked particles ( $1.3 \leq t [\text{s}] \leq 1.6$ ). The

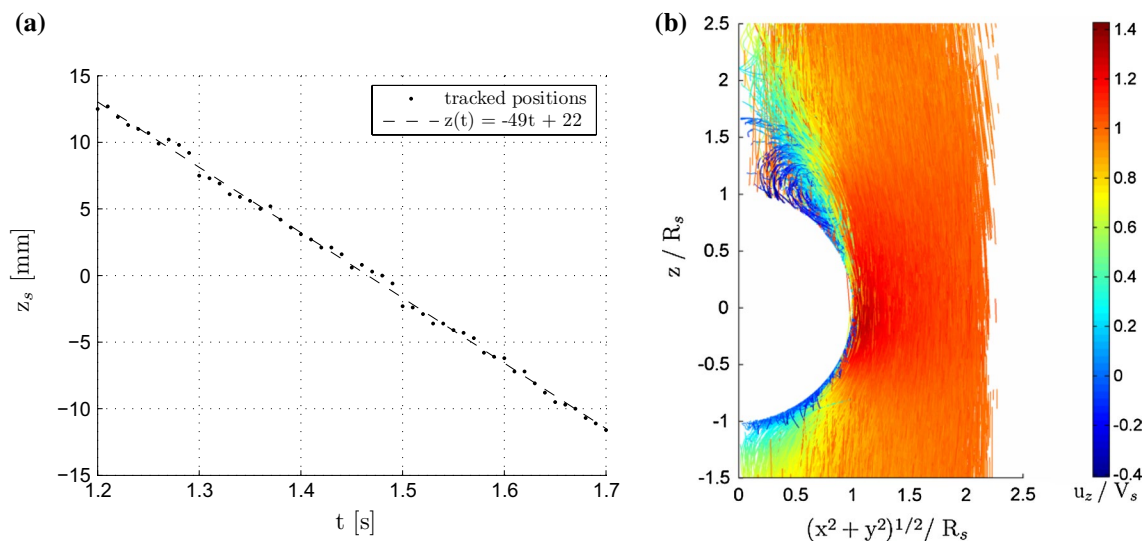


**Fig. 9** **a** The tracked position of the hydrogel sphere in a laboratory-fixed reference frame,  $z_s$ , as it travelled through the measurement domain.  $z_s = 0$  corresponds to the approximate vertical centre of the measurement volume, as defined by the location of the calibration plate. **b** Particle tracks are shown in the reference frame of the

sphere, translated into a cylindrical axisymmetric coordinate system. Tracks are shown for  $1 < t [\text{s}] < 1.5$  and coloured by the ratio of their  $z$ -velocity to the descent velocity of the sphere (or the free-stream velocity in the sphere-centred frame)

pressure was extracted in each frame using the method described in Sect. 1.2, using both the Lagrangian and Eulerian techniques. For the Eulerian technique, the domain was discretized using the same process as was used for the analytical case. Since the pressure was not known at any location in the measurement domain, Neumann boundary conditions were implemented on all domain boundaries. For the Lagrangian case, boundary conditions were handled as such: at the exterior boundaries of the domain, unbound particles were used to explicitly enforce the boundary conditions. At the interior boundaries, artificial boundary particles were added to the flow. These boundary particles were distributed evenly across the spherical surface of the model, for two purposes: first, the even distribution of boundary particles results in a consistent network between the boundary and the surrounding fluid (assuming the particles in the surrounding fluid are evenly distributed). Second, since all boundary particles represent equal proportions of the total surface of the model, integrating across the surface to calculate the pressure force is simplified.

In the Eulerian process, boundary conditions were handled by determining which points in the structured grid aligned with the boundaries of the sphere and exterior boundaries of the measurement domain. Each voxel in the grid was classified as either an interior point, a boundary point, or an exterior point. On interior points, the pressure was iteratively extracted using the Poisson equation, boundary points were used to enforce Neumann boundary conditions, and exterior points were simply disregarded, in both calculations and visualizations. The distance between the centre of a sphere-surface voxel and the centre of the sphere was found to be  $(0.94 \pm 0.03)R_s$ . Given that the side length of a voxel was approximately  $0.14R_s$ , it was assumed that the difference in surface area captured by each voxel could be neglected, and it could be assumed that each voxel captured an approximately equal portion of the sphere's overall surface area. As in the Lagrangian case, this approximation simplifies the process of integrating across the surface to calculate the pressure force.

Before analysing the results of the Lagrangian and Eulerian pressure-field extraction, the issue of the Neumann boundary condition enforcement must be addressed. First, referring again to Fig. 6, it can be observed that the error induced by the Neumann boundary condition implementation is proportional to the normalized pressure gradient normal to the boundary. Therefore, by examining the normalized pressure gradient on the domain boundaries in the experimental data, an approximate assessment can be made of the error which will be induced by the Neumann boundary condition in the experimental Lagrangian pressure extraction.

In the Lagrangian particle field, 80 % of particles which are connected to the sphere boundary points, and

therefore which are used in boundary condition enforcement, have  $|\partial p/\partial n|[R_s/(0.5\rho V_s^2)] < 1.5$ . Furthermore, 80 % of these points which are located either within  $60^\circ$  of the front stagnation point, or trailing point of the sphere have  $|\partial p/\partial n|[R_s/(0.5\rho V_s^2)] < 1$ . Referring to Fig. 6, these normalized pressure gradients normal to the surface of the sphere correspond to  $\Delta C_p \approx 0.25$  and  $\Delta C_p \approx 0.2$ , respectively. On the outer boundary of the measurement domain, 80 % of the particles used to enforce the Neumann boundary condition have  $|\partial p/\partial n|[R_s/(0.5\rho V_s^2)] < 0.5$ , corresponding to an induced pressure-extraction error of  $\Delta C_p < 0.1$ . While it is unavoidable that the enforcement of Neumann boundary conditions will have deleterious effects on the overall estimate of the pressure field, the relatively lower normalized pressure gradients on the domain boundaries in the experimental case indicate that the error induced by the Neumann boundary condition will be less detrimental to the overall pressure-field estimate than in the analytical case.

In the absence of reference data, the extracted pressure fields cannot be quantitatively validated. However, the Lagrangian pressure field can be qualitatively validated by examining its agreement with the Eulerian pressure field as well as the flow field topology. Figure 10 shows slices and axisymmetric views of the pressure field for  $t = 1.4$  s, for both the Lagrangian and Eulerian cases. Qualitatively, the pressure fields are in good agreement and are both of the general form that would be expected based on Fig. 9b: at the leading stagnation point of the sphere, the pressure is approximately  $C_p \approx 1$ . As fluid accelerates around the sides of the sphere, a pressure minima can be observed ninety degrees from the front stagnation point. In the free-stream far from the sphere, the pressure approaches  $C_p \approx 0$ , as expected. There is a severe spatial particle density deficit in the near-wake of the sphere. This deficit is caused primarily by 'streaking' in the raw camera images, which is a blurring or smearing of particle images that occurs when the particle velocities approach or exceed the maximum trackable velocity. This deficit in spatial particle density makes it difficult to comment on the structure of the pressure in this region, for the Lagrangian case.

Additionally, it should be noted that the structured grid used for the Eulerian pressure-extraction procedure was uniform throughout the domain. In the near-wake zone, where a dearth of Lagrangian particles is observed, values interpolated to the structured grid will suffer additional interpolations errors due to oversampling. Because of this oversampling error, the Eulerian pressure-field estimates in the near-wake zone are likely to be much less accurate than in the rest of the domain. However, it can be observed in both cases that as fluid moves from the sides of the sphere into the wake, the pressure appears to be increasing from the observed pressure minima towards the free-stream pressure.

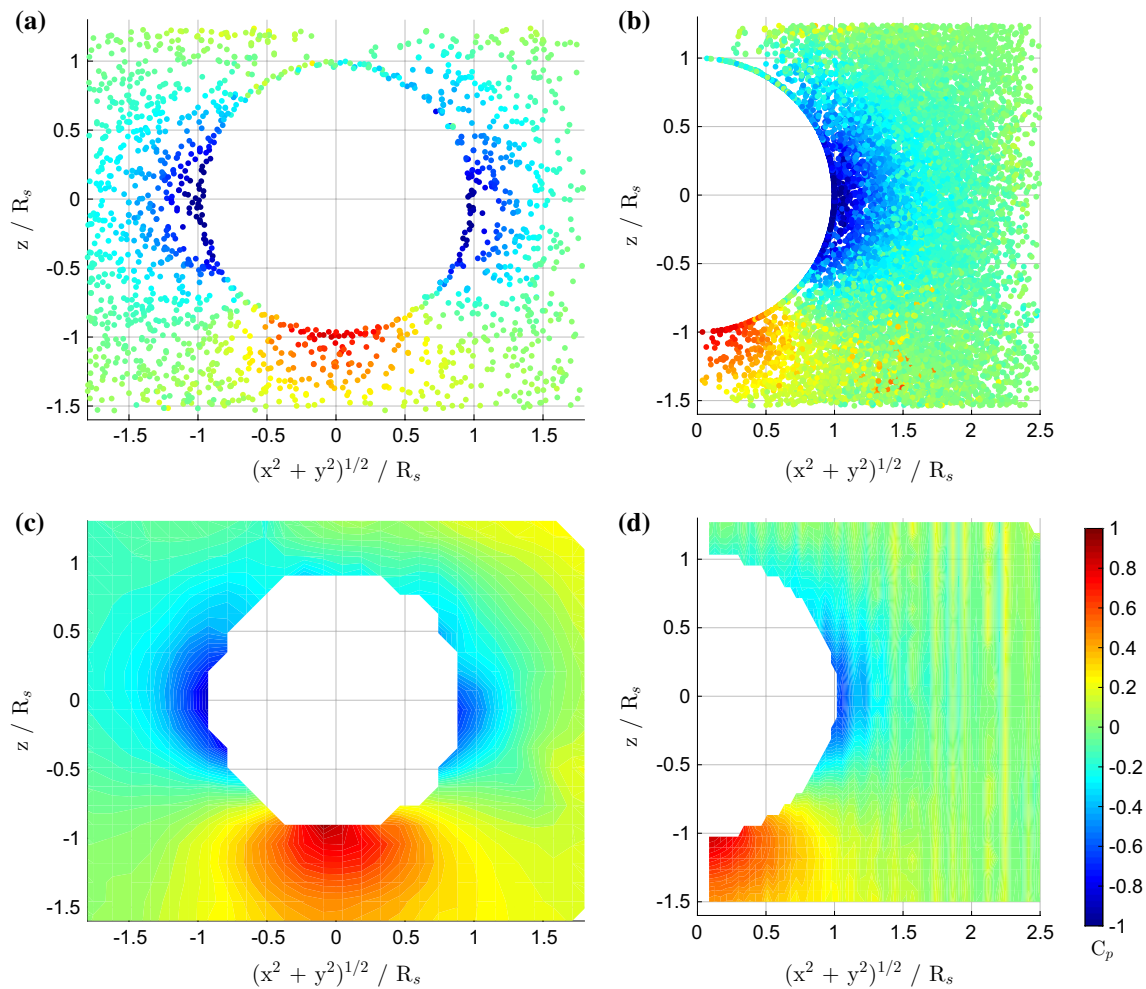


**Fig. 10** Sample pressure coefficient fields are shown in the reference frame of the sphere at  $t = 1.4$  s for: **a** Lagrangian slice in  $xz$ -plane, **b** Lagrangian axisymmetric, **c** Eulerian slice in  $xz$ -plane, **d** Eulerian axisymmetric. The bounds of the Lagrangian and Eulerian slices are  $|y| < 0.3R_s$  (bounds required to display sufficient number of particles)

To further compare the Lagrangian and Eulerian techniques, the distribution of the pressure field on the surface of the sphere can be examined. Figure 11 shows plots of the pressure coefficient versus the angular distance from the front stagnation point, for the Lagrangian and the Eulerian cases. Qualitatively, the form of the pressure distribution is quite similar for the two cases—as observed in the analysis of the pressure field, the pressure is  $C_p \approx 1$  at the stagnation point, gradually drops to a pressure minima approximately ninety degrees from the stagnation point, and trends back towards the free-stream pressure towards the trailing point. However, quantitative differences between the two distributions can be observed as well. In the Lagrangian case, the pressure minima is within the range of  $-1 \leq C_p \leq -0.5$ , while in the Eulerian case, the pressure minima is within the range of  $-0.6 \leq C_p \leq -0.2$ . Additionally, while in the

and  $|y| < 0.13R_s$  (width of a voxel in  $y$ ), respectively. A particle density deficiency can be observed in the regions near the trailing point on the sphere, which would adversely impact the accuracy of the extracted pressure field in the near-wake

Eulerian case the pressure converges on  $C_p \approx 0$  approximately  $150^\circ$  from the front stagnation point, this convergence is not observed in the Lagrangian case. Beyond  $150^\circ$  from the front stagnation point, the pressure field is scattered and inaccurate in both cases. This is expected, as the dearth of Lagrangian particles in the region around the trailing point of the sphere elevates the pressure-extraction error in this region, as previously discussed.

In the absence of reference data, it cannot be determined whether the Lagrangian technique has incorrectly underestimated the value of the pressure minima, or whether the Eulerian technique has incorrectly overestimated the value of the pressure minima. It can, however, be noted that in the Lagrangian technique, every boundary point placed on the surface of the sphere was located precisely on the surface of the sphere. In the Eulerian case, the boundary points

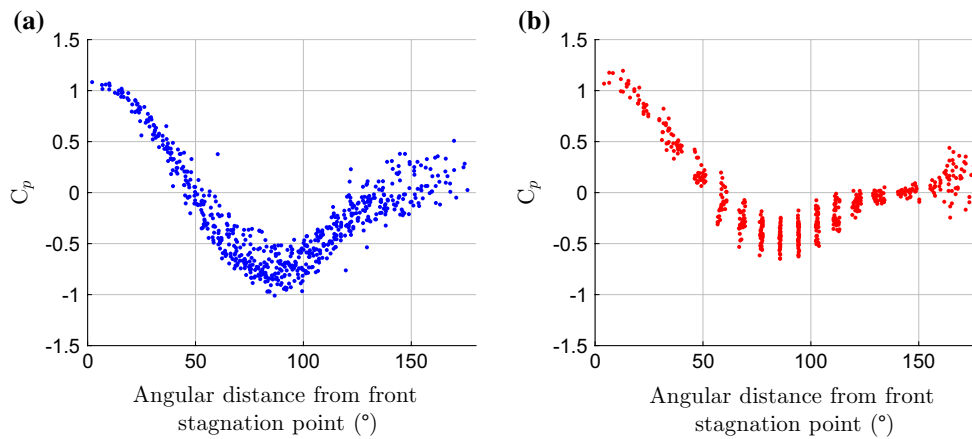


**Fig. 11** The pressure-field distribution on the surface of the sphere at  $t = 1.4$  s is shown in the form of the pressure coefficient as a function of the angular distance from the leading stagnation point, for **a** the Lagrangian case, and **b** the Eulerian case

representing the surface of the sphere are limited to locations where the structured grid is intersected by the surface of the sphere, resulting in less accurate positioning of the boundary points. Additionally, in the Lagrangian technique, fluid particles measured very close to the surface will allow for more accurate gradients to be calculated in the vicinity of the sphere’s surface, when compared to interpolating the flow quantities to a non-refined structured grid near a wall (Kähler et al. 2012). With all of these factors in mind, it can be stated that, while we do not know for certain which technique has provided a better estimate of the pressure minima on the surface of the sphere, there are several factors which would indicate that the Lagrangian technique is likely to provide a better estimate of the pressure field near the surface of the sphere.

### 3.4 Experimental results: drag coefficient comparison

Finally, the estimated drag from the pressure force on the sphere was compared to estimates from the literature for a drag on a sphere at a Reynolds number of  $Re \approx 2100$ , for both cases. The pressure-drag force was evaluated in each frame where the sphere was both fully contained in the measurement volume and surrounded by tracked particles. The pressure force on the sphere was estimated by integrating the pressure over the surface of the sphere:

$$\mathbf{F}_p = - \int_{\partial S} p \mathbf{dA}, \tag{29}$$

where  $\mathbf{F}_p$  is the vector pressure force, and  $\mathbf{dA}$  is an infinitesimal vector area element pointing outwards from the sphere’s surface. Since the surface area of the sphere corresponding to each data point on the sphere is approximately constant, for both the Lagrangian and Eulerian case, this integral can be easily discretized:

$$\mathbf{F}_p = - \frac{4\pi R_S^2}{N} \sum_i^N (p_i \hat{\mathbf{n}}_i), \tag{30}$$

where  $N$  is the number of points on the boundary,  $i$  is an index to sum over,  $p_i$  is the pressure at boundary point  $i$ , and  $\hat{\mathbf{n}}_i$  is the normal unit vector pointing out from the sphere surface at boundary point  $i$ . Finally, the drag force is the component of the force aligned with the direction of motion of the sphere. Therefore, the drag coefficient was calculated for each frame as:

$$C_{D,p} = \frac{\hat{\mathbf{e}}_z \cdot \mathbf{F}_p}{(1/2)\rho V_S^2 (\pi R_S^2)}, \tag{31}$$

where  $\hat{\mathbf{e}}_z$  is the Cartesian basis vector aligned with the direction of motion of the sphere. Using this procedure, the pressure drag on the sphere was calculated for  $1.3 \leq t [s] \leq 1.6$ , and the estimate of the coefficient of pressure drag on the sphere was  $C_D = 0.32 \pm 0.07$  using the Lagrangian pressure fields, and  $C_D = 0.34 \pm 0.07$  using the Eulerian pressure fields. This is an excellent agreement between the two pressure-field extraction techniques, and further serves to validate the results of the novel Lagrangian pressure-extraction technique.

A model for the relationship between drag coefficient and Reynolds number for a falling sphere was recently proposed by Brown and Lawler (2003):

$$C_D = \frac{24}{Re} \left( 1 + 0.150 Re^{0.681} \right) + \frac{0.407}{\left( 1 + \frac{8710}{Re} \right)}. \tag{32}$$

Based on this model, for a sphere falling at a Reynolds number of  $Re \approx 2100$ , the expected drag coefficient is  $C_D \approx 0.404$ . The estimated drag coefficients from the



Lagrangian and Eulerian pressure fields predict the drag coefficient to within two and one standard deviations of this reference value, respectively. However, it should be noted that this is a comparison of a total drag coefficient, from literature, to the pressure force component of the drag coefficient in the experiments. Since the Reynolds number is  $Re \approx 2100$ , it can be reasonably assumed that the pressure force contribution to the drag will be dominant, but the viscous skin friction contribution cannot be totally neglected. With the current experimental dataset, it is not possible to reliably extract, or estimate, the contribution of skin friction to the total drag across the body. Therefore, the comparison to the reference value of drag can be used to demonstrate that the drag force coefficient estimates from the pressure fields are qualitatively reasonable, but cannot be used for a quantitative evaluation.

#### 4 Conclusions

The present investigation uses an analytical test case and dense 4D-PTV data to verify and validate a novel technique for Lagrangian pressure extraction, developed by Neeteson and Rival (2015). This technique utilizes the Delaunay triangulation and Voronoi tessellation to construct a network on a field of scattered particles, allowing vector calculus operations to be performed without interpolating data to a structured grid. Using this network, the pressure is extracted by iteratively solving Poisson's equation for pressure in a discrete Lagrangian frame. The purpose of the current study was to further evaluate and validate the technique. The proposed Lagrangian pressure-extraction technique was compared to the standard Eulerian pressure-extraction technique for an analytical case and an experimental case. The analytical case was the semi-three-dimensional Taylor–Green vortex, and for the experimental test case, 4D-PTV data of the flow around a free-falling sphere were used.

Based on the results of the analytical and experimental test cases, three main conclusions can be drawn:

First, the proposed Lagrangian pressure-extraction technique has been shown to be superior to the typical Eulerian pressure-extraction technique when applied to analytical data with Dirichlet boundary conditions, and it can be reasonably concluded that, given Dirichlet boundary conditions and a Lagrangian dataset with approximately evenly distributed particles, the Lagrangian pressure-extraction technique will provide a more accurate estimate of the pressure field than the standard Eulerian pressure-extraction technique.

Second, the proposed Lagrangian pressure-extraction technique was shown to produce a pressure field in close agreement with that of the Eulerian pressure-extraction

technique when applied to experimental data with Neumann boundary conditions. Since the Eulerian pressure-extraction technique has been used extensively in the literature, the agreement between the two functions as a validation of the proposed Lagrangian pressure-extraction technique, even with the current sub-optimal implementation of the Neumann boundary condition.

Finally, it can be concluded that while the proposed Lagrangian pressure-extraction technique cannot currently be described as superior to existing Eulerian techniques, the results of the experimental analysis clearly demonstrate its validity, while the results of the analytical test case demonstrates the potential of the technique, and inform the direction of future investigation into the technique. Specifically, it is imperative that the issues with the implementation of the Neumann boundary condition are identified and rectified, and moving forward, it will be necessary to utilize a canonical flow case to quantitatively assess the precision error in pressure-field estimates from experimental data. As Lagrangian flow measurement techniques continue to improve and become more widely adopted, the sustained development and investigation into specialized Lagrangian analysis techniques will allow researchers to fully exploit the unique advantages of Lagrangian flow data.

**Acknowledgments** The authors would like to thank Alberta Innovates Technology Futures for their financial backing, and the members of the NIOPLEX research consortium (7th Framework Programme of the European Commission under Grant Agreement 605151) for their valuable feedback.

#### References

- Aurenhammer F (1991) Voronoi diagrams—a survey of a fundamental geometric data structure. *ACM Comput Surv* 23(3):345–404
- Auteri F, Carini M, Zagaglia D, Montagnani D, Gibertini G, Merz CB, Zanotti A (2015) A novel approach for reconstructing pressure from PIV velocity measurements. *Exp Fluids* 56(2):45
- Brachet ME (1991) Direct simulation of three-dimensional turbulence in the Taylor-Green vortex. *Fluid Dyn Res* 8:1–8
- Brachet ME, Meiron DI, Orszag SA, Nickel BG, Morf RH, Frisch U (1983) Small-scale structure of the Taylor-Green vortex. *J Fluid Mech* 130:411–452
- Brown PP, Lawler DF (2003) Sphere drag and settling velocity revisited. *J Environ Eng* 129:222–231
- Cornic P, Champagnat F, Cheminet A, Leclaire B, Besnerais GL (2015) Fast and efficient particle reconstruction on a 3D grid using sparsity. *Exp Fluids* 56:62
- Fujisawa N, Tanahashi S, Srinivas K (2005) Evaluation of pressure field and fluid forces on a circular cylinder with and without rotational oscillation using velocity data from PIV measurement. *Meas Sci Technol* 16:989
- Gurka R, Liberzon A, Hefetz D, Rubinstein D, Shavit U (1999) Computation of pressure distribution using PIV velocity data. PIV'99, Santa Barbara, CA
- Hengl T (2006) Finding the right pixel size. *Comput Geosci* 32(9):1283–1298

- Jeon YJ, Chatellier L, David L (2014) Fluid trajectory evaluation based on an ensemble-averaged cross-correlation in time-resolved PIV. *Exp Fluids* 55:1766
- Kähler CJ, Scharnowski S, Cierpka C (2012) On the uncertainty of digital PIV and PTV near walls. *Exp Fluids* 52:1641–1656
- Laskari A, de Kat R, Ganapathisubramani B (2014) Full-field pressure from 3D PIV snapshots in convective turbulent flow. In: 17th International symposium on applications of laser techniques to fluid mechanics, Lisbon, Portugal
- Lüthi B, Tsinober A, Kinzelbach W (2005) Lagrangian measurement of vorticity dynamics in turbulent flow. *J Fluid Mech* 528:87–118
- Lynch KP, Scarano F (2015) An efficient and accurate approach to time-resolved tomographic PIV. *Exp Fluids* 56:66
- Neeteson NJ, Rival DE (2015) Pressure-field extraction on unstructured flow data using a voronoi tessellation-based networking algorithm: a proof-of-principle study. *Exp Fluids* 56(44):1–13
- Novara M, Scarano F (2013) A particle-tracking approach for accurate material derivative measurements with tomographic PIV. *Exp Fluids* 54:1584
- Raffel M, Willert CE, Wereley ST, Kompenhans J (2007) Particle image velocimetry: a practical guide, 2nd edn. Springer, New York
- Schanz D, Gesemann S, Schröder A, Wieneke B, Novara M (2013a) Non-uniform optical transfer functions in particle imaging: calibration and application to tomographic reconstruction. *Meas Sci Technol* 24(2):024009. doi:10.1088/0957-0233/24/2/024009
- Schanz D, Schröder A, Gesemann S, Michaelis D, Wieneke B (2013b) Shake the box: a highly efficient and accurate tomographic particle tracking velocimetry (TOMO-PTV) method using prediction of particle positions. In: 10th International symposium on particle image velocimetry, Delft, The Netherlands
- Schanz D, Schröder A, Gesemann S (2014) Shake the box—a 4D PTV algorithm: accurate and ghostless reconstruction of Lagrangian tracks in densely seeded flows. In: 17th International symposium on applications of laser techniques to fluid mechanics, Lisbon, Portugal
- Schneiders JFG, Lynch K, Dwight RP, van Oudheusden BW, Scarano F (2014) Instantaneous pressure from single snapshot tomographic PIV by Vortex-in-Cell. In: 17th International symposium on applications of laser techniques to fluid mechanics, Lisbon, Portugal
- Shu CW, Don WS, Gottlieb D, Schilling O, Jameson L (2005) Numerical convergence study of nearly incompressible, inviscid Taylor-Green vortex flow. *J Sci Comput* 24(1):1–27
- Sibson R (1981) A brief description of natural neighbor interpolation (chapter 2). In: Barnett V (ed) *Interpreting multivariate data (probability and mathematical statistics)*. Wiley, Chichester, pp 21–36
- Sukumar N, Bolander JE (2003) Numerical computation of discrete differential operators on non-uniform grids. *Comput Model Eng Sci* 4:691–706
- Taylor GI, Green AE (1937) Mechanism of the production of small eddies from large ones. *Proc R Soc Lond Math Phys Eng Sci* 158(895):499–521. doi:10.1098/rspa.1937.0036
- van Oudheusden BW (2013) PIV-based pressure measurement. *Meas Sci Technol* 24(032):001
- Violato D, Moore P, Scarano F (2011) Lagrangian and Eulerian pressure field evaluation of rod-airfoil flow from time-resolved tomographic PIV. *Exp Fluids* 50:1057–1070
- Wieneke B (2008) Volume self-calibration for 3D particle image velocimetry. *Exp Fluids* 45:549–556
- Wieneke B (2013) Iterative reconstruction of volumetric particle distribution. *Meas Sci Technol* 24(024):008
- Young D (1950) Iterative methods for solving partial difference equations of elliptic type. Ph.D. thesis, Harvard University